

An investigation of light transport through scattering bodies with non-scattering regions

Michael Firbank[†], Simon R Arridge[‡], Martin Schweiger[†] and David T Delpy[†]

[†] Department of Medical Physics and Bioengineering, University College London, 11–20 Capper Street, London WC1E 6JA, UK

[‡] Department of Computer Science, University College London, Gower Street, London WC1E 6BT, UK

Received 18 August 1995, in final form 9 January 1996

Abstract. Near-infra-red (NIR) spectroscopy is increasingly being used for monitoring cerebral oxygenation and haemodynamics. One current concern is the effect of the clear cerebrospinal fluid upon the distribution of light in the head.

There are difficulties in modelling clear layers in scattering systems. The Monte Carlo model should handle clear regions accurately, but is too slow to be used for realistic geometries. The diffusion equation can be solved quickly for realistic geometries, but is only valid in scattering regions.

In this paper we describe experiments carried out on a solid slab phantom to investigate the effect of clear regions. The experimental results were compared with the different models of light propagation. We found that the presence of a clear layer had a significant effect upon the light distribution, which was modelled correctly by Monte Carlo techniques, but not by diffusion theory.

A novel approach to calculating the light transport was developed, using diffusion theory to analyse the scattering regions combined with a radiosity approach to analyse the propagation through the clear region. Results from this approach were found to agree with both the Monte Carlo and experimental data.

1. Introduction

Near-infra-red (NIR) spectroscopy is currently being widely used to measure changes in the oxygenation of cerebral and other tissues of both neonates and adults (Wyatt *et al* 1986, Edwards *et al* 1988, Hampson and Piantadosi 1988, Peebles *et al* 1992, Elwell *et al* 1993, De Blasi *et al* 1993). It is not certain, however, exactly which parts of the tissue are being interrogated by the technique. This uncertainty is caused by the scattering and inhomogeneous nature of tissue. The scattering nature of tissue can be modelled using either Monte Carlo or diffusion models of light transport and several studies have used these models to investigate light propagation in homogeneous objects (Patterson *et al* 1989, Flock *et al* 1989, Key *et al* 1991, Arridge *et al* 1992). Some further theoretical studies have been reported in the literature which investigate the effect of tissue inhomogeneity, using models in which there are two or more layers with different optical properties (van Gemert *et al* 1989, Haselgrove *et al* 1992, Hiraoka *et al* 1993). All of these studies have, however, only considered situations in which all the layers scatter light by varying amounts, and there have not been (to our knowledge) any studies of the effect of non-scattering (clear) layers.

An examination of the effect of clear layers is particularly important in considering the use of NIR spectroscopy on the head. In this case, a clear layer of cerebrospinal fluid (CSF) forms a boundary between the outside tissues (skull and scalp) and the brain. Due to the convoluted nature of the brain, the thickness of the CSF varies between about 1 and 10 mm. In order to be able to fully interpret the results of NIR studies on the head, it is necessary to know what percentage of the detected light has passed through the brain and where within the tissues it has travelled.

We have investigated this situation using both experimental data measured upon a simple phantom, and theoretical predictions from both Monte Carlo and a finite-element model based on diffusion theory. The situation investigated was a simple slab geometry, with a clear region of varying thickness confined between two scattering layers.

An algorithm based on a radiosity approach, which specifically calculates light transport across clear regions, was developed. Using a combination of this algorithm and the diffusion equation allows fast calculation of light intensities in scattering bodies with clear regions.

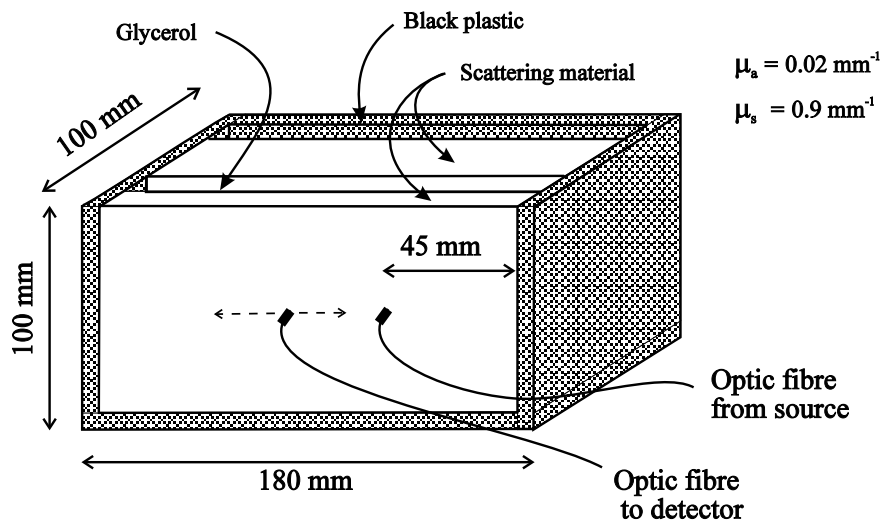


Figure 1. The experimental phantom and measurement setup.

2. Experimental setup

The phantom (see figure 1) consists of two slabs of scattering material. Both slabs are 17 cm wide by 10 cm high, but the first is 1 cm thick, and the second 7 cm thick. The 1 cm thick slab forms the front end of a watertight box, whose other walls are made of opaque black plastic. The box is filled with glycerol, and the thicker slab sits inside the box and can be positioned at a variable distance away from the front slab.

The scattering material is a clear epoxy resin into which have been added 1 μm diameter amorphous silica spheres (Monospher: Merck, Germany) and absorbing dyes (Firbank *et al* 1995a, Firbank 1994). The quantity of spheres present determines the transport scattering coefficient, $\mu'_s = (1-g)\mu_s$, μ_s being the scattering coefficient, and g being the mean cosine of scattered light. In this phantom, $\mu'_s = 0.9 \text{ mm}^{-1}$ at 800 nm, the g value being 0.92. The scattering coefficient is the same in the two slabs. The epoxy has a refractive index n_d of 1.57, and glycerol an n_d of 1.47. The ratio of these two indices is approximately the same

as the ratio of CSF ($n_d \sim 1.33$) to brain tissue ($n_d \sim 1.4$). The absorption coefficient μ_a is determined by the amount of dye added to the plastic and by the absorption spectrum of the epoxy resin. The slabs contain infra-red absorbing dye (Projet 900NP: Zeneca Ltd, Manchester, UK). The absorption spectra of the resin and of the dye at the concentration used in the phantom are shown in figure 2.

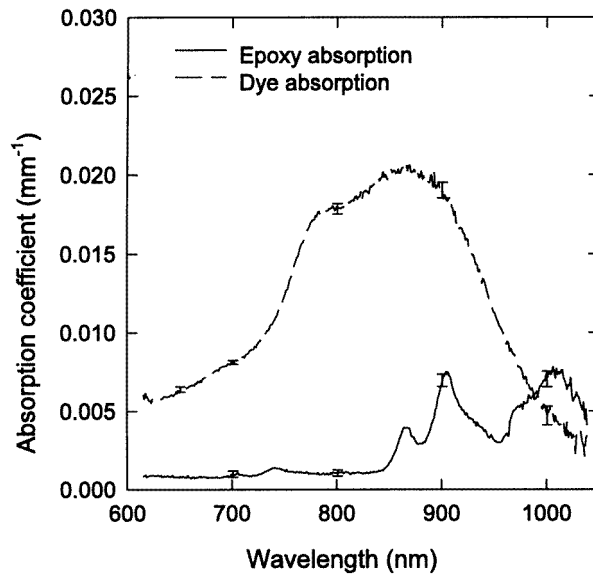


Figure 2. The absorption spectra of the epoxy resin and the dye used in the phantom. Error bars, ± 1 SD.

To determine approximate values for the optical coefficients of the head, data from the temporal distribution of light measured through the heads of seven volunteers (Matcher *et al* 1995) were taken and fitted to the homogeneous diffusion equation (Arridge *et al* 1992), using the absorption and scattering coefficients as variable parameters. The mean values obtained from this fitting at 800 nm were $\mu_a = 0.02 \text{ mm}^{-1}$, $\mu'_s = 0.9 \text{ mm}^{-1}$. For comparison, the mean value of μ_a for the outer and inner scattering layers of the phantom was 0.02 mm^{-1} over 700–900 nm. The absorption of glycerol (0.003 mm^{-1} at 800 nm) is comparable to water (0.0033 mm^{-1} at 800 nm) (Hale and Querry 1973).

3. Measurements

Experiments were performed with different spacings between the front and back slabs, ranging from zero up to 10 mm. Measurements were also made on the thicker slab by itself, in order to provide comparative data from a homogeneous slab. Measurements were made to determine both the mean time of flight and the intensity of the reflected light as the source–detector spacing varied. The reflected intensity as a function of wavelength was ascertained using a quartz halogen white light source (Oriel, CN, USA) and a cooled spectrographic CCD detector (Cope *et al* 1989). Light was carried along an optical fibre bundle (2 mm in diameter), which had one end illuminating the front surface of the phantom, 4.5 cm from the bottom and left hand sides (see figure 1). A second optical fibre bundle

carried reflected light to the detector. This fibre was held on a stepper motor controlled stage, and moved in 2 mm steps to alter the spacing between the two fibres from 15 to 45 mm. Measurements were made at each step, and covered the wavelength range 650–1000 nm. A separate measurement was made without the phantom present, with the light source directly illuminating the fibre, to determine the input light spectrum.

To measure the mean time of flight of the light, a streak camera (C1587: Hamamatsu Photonics KK, Hamamatsu, Japan) and a pulsed picosecond laser (Tsunami, Spectra-Physics Ltd, CA, USA) were used. Light from the laser at 800 nm directly illuminated the phantom surface, and an optical fibre bundle, again mounted on a motor controlled stage, carried the reflected light to the streak camera detector. A small fraction of the laser beam was directed onto a separate optical fibre connected to the streak camera to provide a time reference. At the start of the experiment, a measurement was made without the phantom present, so that the time at which the photons hit the phantom surface relative to the reference could be determined.

4. Theory

4.1. Determination of pathlength from attenuation measurements

The attenuation of light in a scattering medium can be approximated by a modified form of the Beer–Lambert law (Cope *et al* 1988), provided that the absorption coefficient μ_a stays reasonably constant:

$$\ln(I/I_0) = -\mu_a L + K \quad (1)$$

where I_0 is the incident light, I the detected light, K a geometry dependent constant and L the total mean pathlength through the medium. In the case where there are different absorbers, $\mu_{a1}, \mu_{a2}, \dots$ in regions 1, 2, \dots this can be rewritten as

$$\ln(I/I_0) = -(\mu_{a1}L_1 + \mu_{a2}L_2 + \dots) + K. \quad (2)$$

Hence, by fitting a linear sum of the known absorption spectra and a constant to the measured attenuation spectra of the reflected light, an estimate of the partial pathlengths L_1, L_2, \dots can be made.

Using this equation, we can determine the partial pathlength through the scattering slabs using the epoxy absorption spectrum, and through the clear layer using the glycerol absorption spectrum. If a further dye with a distinctive absorption spectrum were added to the second slab, it would be possible (in principle) to measure the partial pathlength solely through this region.

4.2. The Monte Carlo model

A Monte Carlo model was used to simulate the experimental arrangement. This model (Hiraoka *et al* 1993) stored the path taken by each photon through each of the three different layers. This enabled calculation of the partial pathlength taken through each layer separately, as well as the total pathlength.

The Monte Carlo simulation used isotropic scattering, with a scattering coefficient of 0.89 mm^{-1} and an absorption coefficient of 0.025 mm^{-1} . These are equal to the properties of the slabs at 900 nm. For the clear layer, a μ_a value of 0.02 mm^{-1} was used. The absorption properties were chosen to agree with the peak values of the absorption features, since the pathlength fitting procedure in equation (2) uses the absorption peaks. Hence the clear layer μ_a is higher than that of glycerol at 800 nm, but this only has an effect upon

the partial pathlength in the clear layer. Fresnel reflection boundary conditions were used at the slab–air interface, with a refractive index of 1.56 for the scattering regions. The internal clear region was also assumed to have a refractive index of 1.56, and hence there was no reflection at its boundaries. A more complete model could include a refractive index mismatch at the clear layer boundaries. One million input photons were used in the simulations.

4.3. The diffusion model

In order to model the arrangement using solely the diffusion equation, the finite-element method approach was used. This allows the optical properties to vary in different regions. The finite-element implementation employed (Schweiger *et al* 1993) was a two-dimensional model, and used extrapolated boundary conditions without surface reflection (Farrell and Patterson 1992). The area in question (8 cm × 18 cm) was divided up into a mesh of approximately 35 000 triangular elements. For the scattering regions, the scattering and absorption coefficients were the same as those used in the Monte Carlo simulation. For the clear layer, the value chosen for μ'_s was 0.01 mm⁻¹, whilst μ_a was set to a value of ten times less than this, i.e. 0.001 mm⁻¹. The exact choice of optical parameter was found to be not critical.

4.4. The hybrid radiosity–diffusion theory

In this discussion, we define the radiance $I(p, s, t)$ (units m⁻² s⁻¹ sr⁻¹) as the number of photons at position p travelling in direction s per unit area at time t . The fluence rate $\phi(p, t)$, is then given by

$$\phi(p, t) = \int \int_{4\pi} I(p, s, t) d\Omega. \quad (3)$$

This quantity is estimated by the time dependent diffusion equation:

$$(1/c)d\phi(p, t)/dt - \nabla\kappa(p)\nabla\phi(p, t) + \mu_a(p)\phi(p, t) = q_0(p, t) \quad (4)$$

where q_0 is the source, and the diffusion coefficient $\kappa(p)$ is given by

$$\kappa(p) = 1/3[\mu_a(p) + \mu'_s(p)]. \quad (5)$$

The fluence $\phi(p)$ is given by the integral of the fluence rate over all time.

The exitance rate $\Gamma^e(p, t)$ is defined as the number of photons passing outwards through an area dA per second:

$$\Gamma^e(p, t) = \int \int_{2\pi} I(p, s, t) \cdot \hat{n} d\Omega \quad (6)$$

where \hat{n} is the normal to dA .

The irradiance rate $\Gamma^i(p, t)$ is similarly defined as the number of incoming photons per unit area per second.

The exitance rate can be calculated from the diffusion equation thus:

$$\Gamma^e(p, t) = -\kappa(p)\hat{n} \cdot \nabla\phi(p, t). \quad (7)$$

The irradiance $\Gamma^i(p)$ and exitance $\Gamma^e(p)$ are defined respectively as the integrals of the irradiance rate and exitance rate over all time.

Radiosity (Cohen and Wallace 1993) is the name for a technique in computer image simulation which allows the calculation of the irradiance on a surface from a light source (e.g. a point on another surface) at a distance r and angle θ_2 (see figure 3). In our case, we

wish to calculate the irradiance on surface 2 from the whole of surface 1. We can find this irradiance $\Gamma_2^i(q)$ on an area dA at position q , by integrating the contribution from all over the first surface A_1 .

$$\Gamma_2^i(q) = \iint_{A_1} \frac{I_1(p, \mathbf{r}) \cos(\theta_1) \cos(\theta_2)}{|\mathbf{r}|^2} dA_1. \quad (8)$$

$I_1(p, \mathbf{r})$ is the outgoing radiance from surface 1, \mathbf{r} being the vector pointing from p to q .

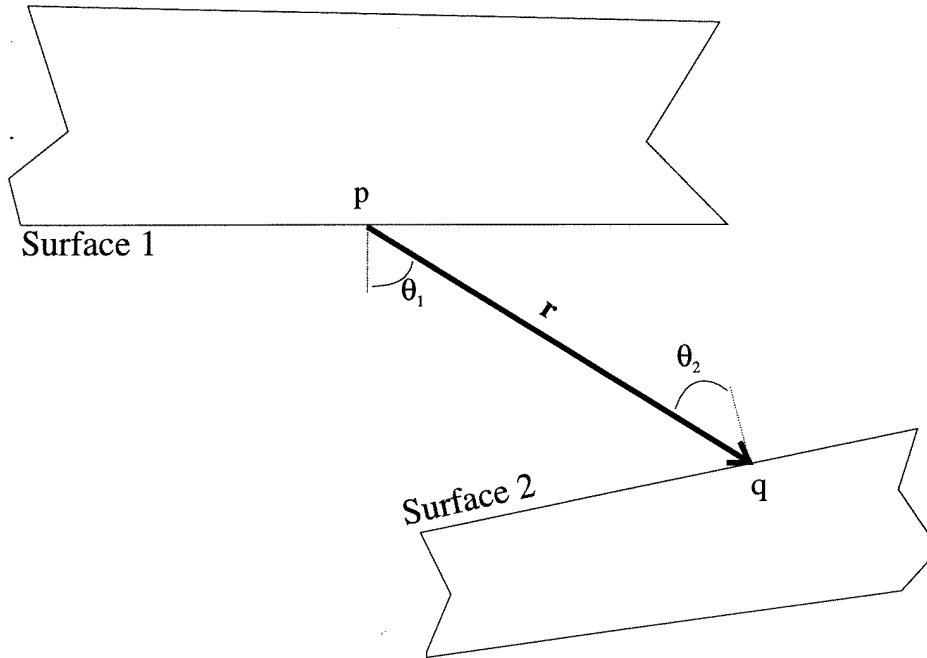


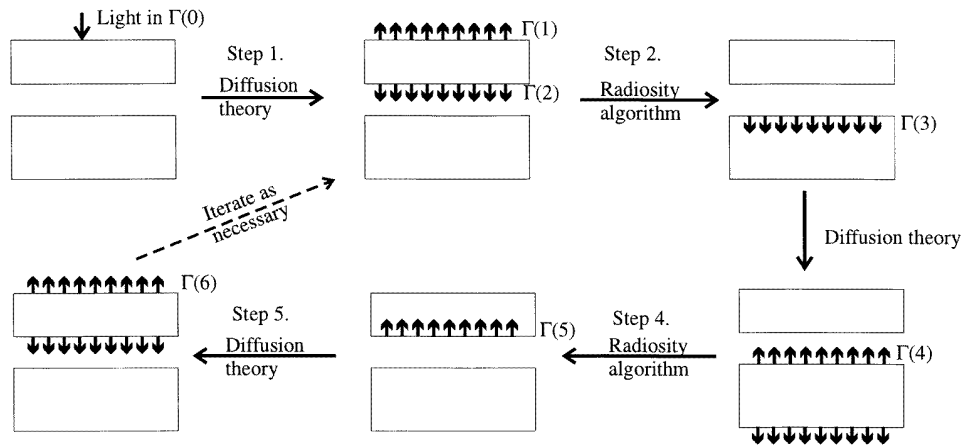
Figure 3. The geometry used for the radiosity equation.

In the case of the clear layer having an absorption coefficient μ_a , this expression will be simply modified to

$$\Gamma_2^i(q) = \iint_{A_1} \frac{I_1(p, \mathbf{r}) \cos(\theta_1) \cos(\theta_2)}{|\mathbf{r}|^2} \exp(-|\mathbf{r}| \mu_a) dA_1. \quad (9)$$

The angular dependence of the outgoing radiance $I_1(p, \mathbf{r})$ is discussed in the next section.

For our calculations of the hybrid radiosity–diffusion theory, the integrations in equation (9) were performed by dividing each of the surfaces up into an 150×150 array of 1 mm^2 pixels. As shown in figure 4, diffusion theory was used to calculate the exitance on the surface of the first region at each of these pixels. The radiosity equation (9) was then used to calculate the irradiance at each pixel on the second surface. Each of these pixels then acted as a source for a diffusion theory calculation of the light distribution in the lower scattering slab, the exitance at each pixel being a sum of the diffuse light from every other pixel. The resulting exitance from the slab surface was then used as an input to the radiosity equation, which calculated the irradiance onto the first surface, and again each pixel acted as a source for a separate diffusion calculation of the light distribution in



Steps 2 - 5 can be repeated until the solution converges.
 Outgoing light = $\Gamma(1) + \Gamma(6) + \dots$

Figure 4. Steps in the combined diffusion-radiosity calculation.

the first slab, and the exitance from each source was summed. This process was iterated until the change to the total exitance on the output surface became negligible.

To calculate the mean time of flight, a similar approach was taken. The mean time of flight on surface 1 was calculated using diffusion theory (Arridge *et al* 1992). The time taken for the light to pass through the clear layer is simply given by

$$t = (r/c)n \tag{10}$$

where c is the speed of light (*in vacuo*) and n the refractive index.

The mean time of flight to a point on surface 2 is then given by summing all the contributions from surface 1 thus:

$$\langle r \rangle = \left(\sum_{n=0}^N (\langle t_n \rangle + t'_n) \Gamma_n^i \right) / \sum_{n=0}^N \Gamma_n^i \tag{11}$$

where $\langle t_n \rangle$ is the mean time at pixel n on surface 1, t'_n is the time from pixel n to the pixel of interest on surface 2, and Γ_n^i is the irradiance at that pixel on surface 2 due to pixel n on surface 1.

From this mean time distribution, the diffusion theory was used to calculate the mean time at each point k on the second surface by summing the contribution from every pixel j on the same surface, after the light had been scattered in the slab:

$$\langle t_k \rangle = \left(\sum_{j=0}^J (\langle t_j \rangle + \langle t_{jk} \rangle) \Gamma_{jk}^e \right) / \sum_{j=0}^J \Gamma_{jk}^e \tag{12}$$

where $\langle t_j \rangle$ is the incident mean time at pixel j , Γ_{jk}^e the exitance at pixel k from j , and $\langle t_{jk} \rangle$ the mean time delay from j to k .

Equation (11) was used to calculate the time delay back across the clear layer, and then the diffusion equation used in a similar fashion for the time distribution in the first slab. Again, this process was iterated until further iterations had negligible effect (which

we defined as the point where the last iteration changed the total exitance and mean time by less than 1%).

Any solution of the diffusion equation, including the finite-element method can be used with these radiosity equations; in the simple slab case investigated here, analytical solution of the diffusion equation was available. The mean time, reflected and transmitted intensities on the first layer were calculated from the (3D) analytical Green function solution to the diffusion equation for an infinite slab. For the third layer, the Green function for an infinite half space was used (Arridge *et al* 1992). The model employed extrapolated boundary conditions without surface reflection, and the same optical properties as the Monte Carlo model. Seven iterations were found to be necessary for a 1 cm clear layer. This varied a little depending on the thickness of the clear layer, thinner clear layers requiring more iterations. This is probably due to the more rapid outward spreading of the light in thicker clear layers.

4.5. The emergent angular distribution

To use the radiosity equation, the emergent radiance of the light exiting from the first surface must be known. This problem has previously been considered in stellar physics, and some researchers have investigated the problem in the field of tissue optics (Bruscaglioni *et al* 1993, Haskell *et al* 1994, Barbour *et al* 1991), although not completely, and hence we include a discussion here adapted from Mihales (1978).

Consider the photon density inside a scattering body $\phi(p)$ (see figure 5). Assuming that the internal radiance is isotropic, the radiance in any direction is equal to $\phi(p)/4\pi$.

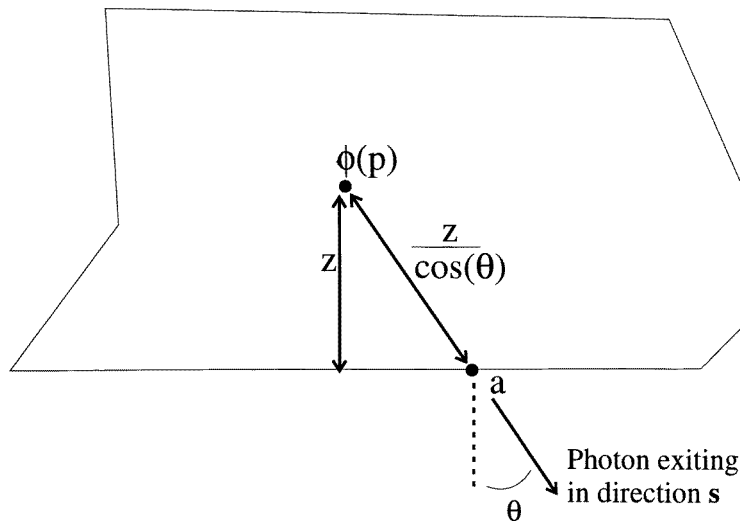


Figure 5. The geometry for emergent photons at point a on the surface of the scattering media.

At a distance from the source, the surface radiance $I(a, s)$ can be found by considering the photons inside the body which are travelling towards that point, and which reach the surface without being scattered or absorbed.

$$I(a, s) = \int_0^\infty \frac{\phi(p)}{4\pi} \exp\left(\frac{-(\mu'_s + \mu_a)z}{\cos(\theta)}\right) \frac{dz}{\cos(\theta)} \quad (13)$$

where the integral is over all points on a line with a in direction s .

To obtain a first approximation to the surface radiance, we assume that the photon density varies linearly with depth into the medium. This linear dependence can be estimated from the extrapolated boundary (where the extrapolated internal intensity falls to zero) which is $0.71/\mu'_s$ outside the medium according to Moulton (1990). Given that $\mu'_s \gg \mu_a$, equation (13) can then be written

$$I(a, s) = \int_0^\infty \frac{\phi(a)}{4\pi \cos(\theta)} \left(1 + \frac{\mu'_s z}{0.71}\right) \exp\left(-\frac{\mu'_s z}{\cos(\theta)}\right) dz = \frac{K(a)}{\mu'_s} \left(1 + \frac{\cos(\theta)}{0.71}\right) \quad (14)$$

where $K(a)$ is proportional to the exitance at a . Figure 6 shows a comparison between $I(a, s) \cos(\theta)$ and the angular distribution of exiting light on the far side of a 1 cm thick slab as calculated by Monte Carlo modelling. The source was a collimated point source at $r = 0$. The photons were binned according to their exiting zenithal angle θ , and the total divided by $\sin(\theta)$ to compensate for the integration around the radius. The μ_a used was 0.025 mm^{-1} , μ'_s 0.9 mm^{-1} and $g = 0$. Two sets of data are shown: from photons exiting opposite the (point) source, and from photons exiting within a radius of 15–20 mm. This simulation used one million photons and had no surface reflection. The distribution that would be expected if the exiting light were isotropically distributed (i.e. $\propto \cos(\theta)$) is also shown for comparison. The data are all normalized by their total area.

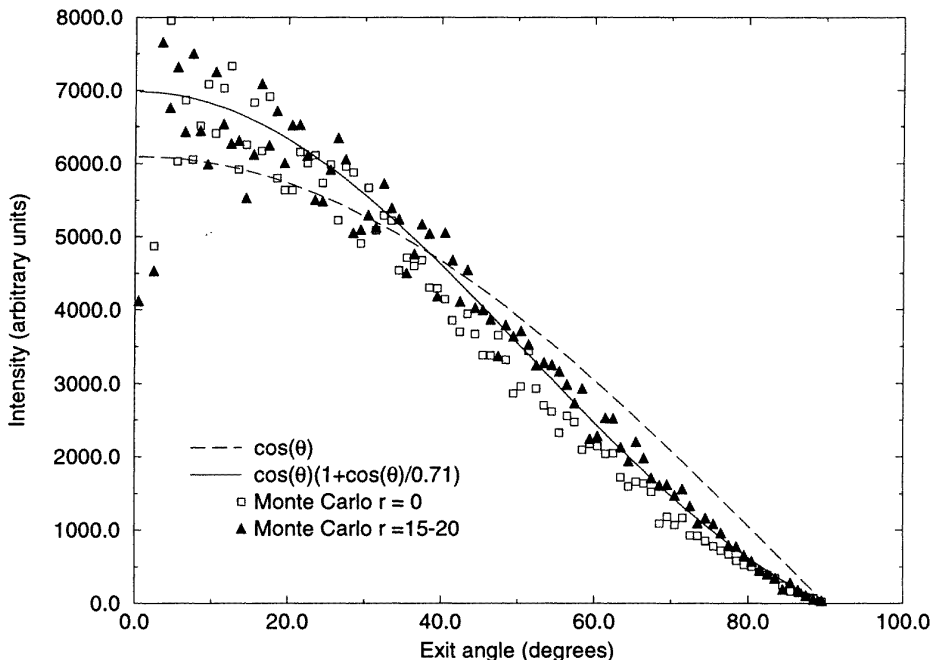


Figure 6. The angular dependence of light exiting from a 10 mm thick slab.

For reflected photons, the angular distribution is Lambertian, being proportional to $\cos(\theta)$. Hence for the radiosity, equation (14) should be used for the first iteration, i.e. light emerging from the far side of the first region from a point source, and for further calculations of the radiosity equation the $\cos(\theta)/0.71$ term should be dropped, as the reflected light is isotropic.

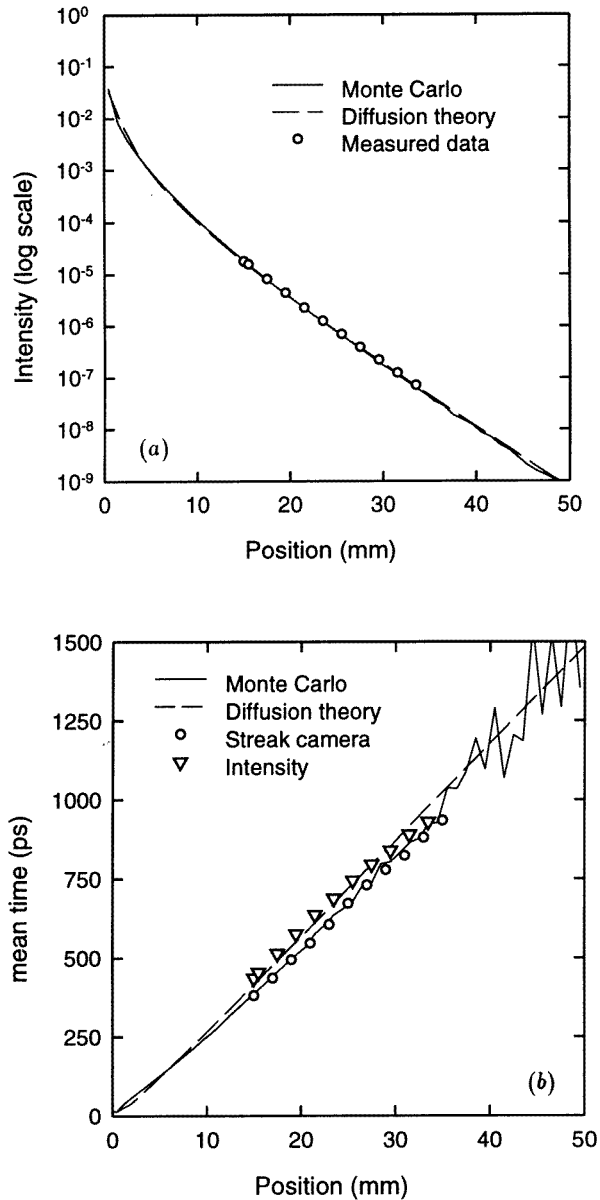


Figure 7. For the case of a homogeneous slab, (a) the measured intensity and (b) the mean time of flight (from streak camera and absorption methods) as a function of fibre spacing compared with that predicted from Monte Carlo and diffusion theory.

5. Results

Figure 7(a) shows the reflected intensity measured on the homogeneous slab as a function of source–detector separation. The results from both the Monte Carlo and diffusion theory models are also shown. The measured data have been scaled to provide the best match

with the modelled data. As expected there is a good agreement between the predictions of the two models and the measured data. Figure 7(b) shows the mean time of flight as measured with the streak camera, and as calculated from the reflectance data using the epoxy absorption spectra. The Monte Carlo and diffusion theory predictions are also shown, and there is again a good agreement between the experimental results and the model predictions.

For the inhomogeneous case of a 1 cm clear layer, figure 8(a) shows similar data for reflected intensity, and figure 8(b) the mean time of flight measured on the phantom with 1 cm of glycerol between the front and back slabs. The results from the Monte Carlo modelling, diffusion theory and hybrid radiosity–diffusion theory are also shown. As can be seen, the Monte Carlo and hybrid model provide results which agree well with the measured data. The diffusion theory alone does not match the experimental results beyond a source–detector separation of 20 mm. Similar measurements were made for a range of different thicknesses of the clear layer, varying from 0.2 to 20 mm. In all cases, a large disparity was noticed between the simple diffusion theory predictions and the experimental, hybrid diffusion–radiosity and Monte Carlo results (which were in good agreement).

Most of the differences between the Monte Carlo and hybrid diffusion models at small distances are due to them having different boundary conditions. The diffusion theory used extrapolated boundary conditions without reflection, whereas the Monte Carlo model used Fresnel reflection at the boundary, which is more realistic. The solution to the diffusion theory can be altered to include reflection at boundaries, but this would be more complicated in this case, as we have a slab with reflection on one side and not on the other. A comparison between the Monte Carlo model without boundary reflection and diffusion theory is shown at the end of this section.

The individual pathlengths through the different regions could only be calculated with Monte Carlo modelling. Figure 9 shows data for a 1 cm clear region between the two slabs. The Monte Carlo calculations of the pathlength through the clear layer, and of the total pathlength through the two scattering layers, are shown as a function of source–detector separation. The pathlengths calculated from the experimentally measured intensity using the known epoxy and glycerol absorption spectra are also shown.

Figure 10 shows the same pathlength data for a 1 mm clear layer between the slabs. Again, we see a good agreement between the modelled pathlengths and those derived from the experimental measurements.

In an attempt to indicate from this simple slab model the likely contribution of brain tissue to the overall signal obtained in NIR spectroscopy of the adult head, figure 11 shows the fractional pathlengths of the detected light in the different regions of the phantom. For source–detector spacings of greater than approximately 30 mm, when there is a 10 mm clear layer, the detected light has spent approximately 10% of its time in the inner slab, and in the case of a 1 mm thick clear layer this increases to 20%. Since the optical properties and thickness of the front layer of this phantom are approximately the same as that of the skin/skull in the human adult, it would imply that in NIR spectroscopy the detected light has spent 10–20% of its time in the brain. It should however be noted that this does not necessarily equate to the signal contributions, since these depend upon the changes in chromophore concentrations in each layer, and the chromophore concentration of the clear layer is of course zero.

To provide a direct comparison between the Monte Carlo and hybrid diffusion/radiosity model, a further calculation was performed with the Monte Carlo model without reflection at the boundaries. Eight million photons were used in this calculation, which took 2 d CPU time to calculate on a Sun Classic Sparc workstation. For the hybrid model shown, the surfaces were divided into an array of 200×200 1 mm² points. Ten iterations of

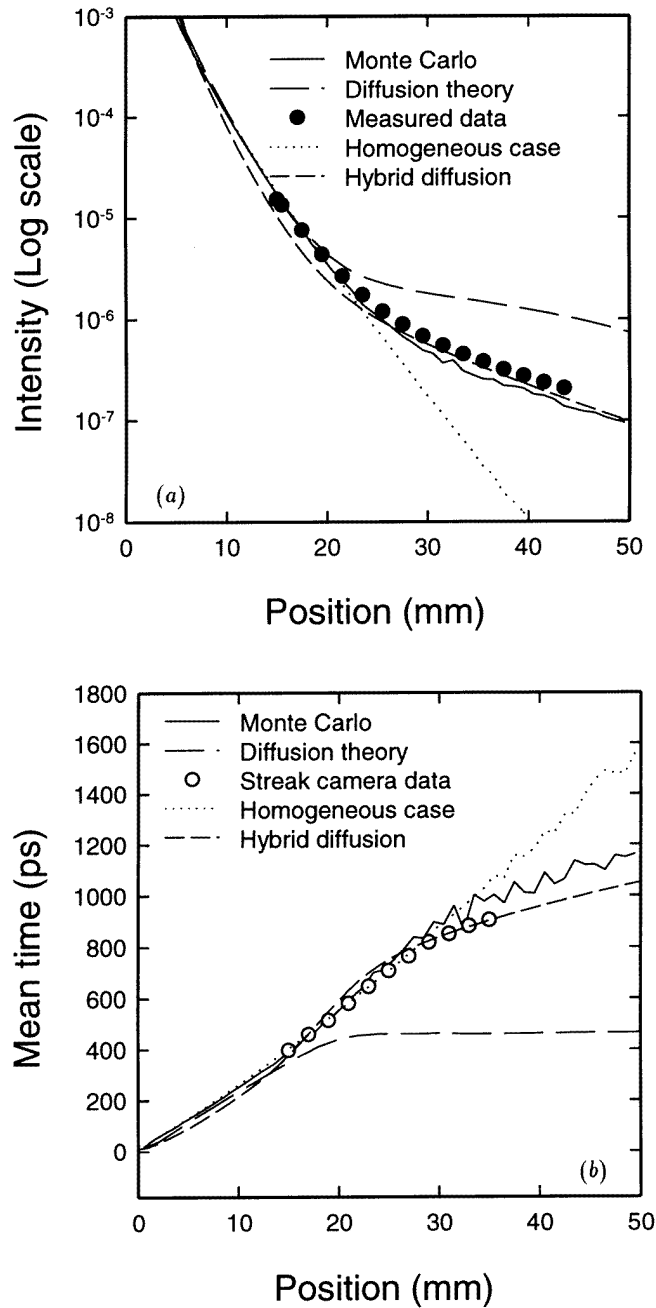


Figure 8. (a) The measured intensity and (b) the mean time of flight as a function of fibre spacing for a 10 mm clear layer compared to Monte Carlo and diffusion calculations and hybrid diffusion–radiosity models. The homogeneous case results are shown for comparison.

the calculation were needed, and this took 20 min of computation time. The clear layer was 1 mm thick. Figure 12(a) shows a comparison between the intensity calculated by

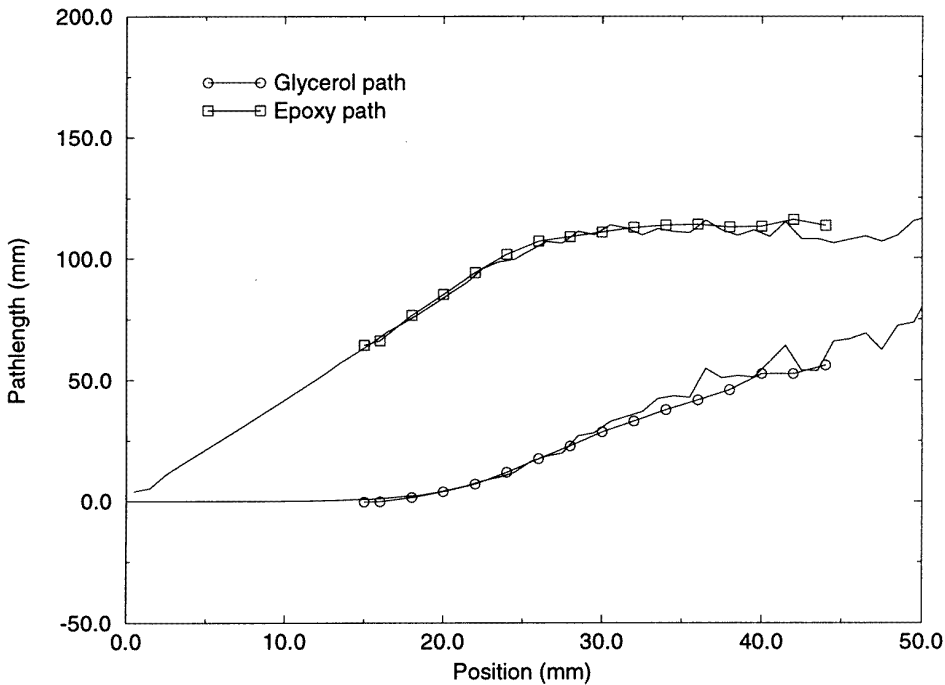


Figure 9. The pathlengths in the scattering and clear media as a function of fibre spacing measured from attenuation spectra compared to Monte Carlo calculations for the case of the 10 mm clear layer.

these two models, and figure 12(b) the mean time of flight. As can be seen there is a good agreement between the two models. It is interesting to see the effect upon the mean time of flight at detector positions greater than 4 cm. The flattening off is probably due to the detected light at these large distances travelling largely through the clear layer. The hybrid diffusion model does tend to underestimate the Monte Carlo predictions of mean time for large distances. This may be due to the approximate nature of the expression for the emergent angular distribution into the clear layer.

6. Conclusions

We have shown that the presence of even a thin non-scattering layer between two scattering regions has a significant effect upon the light distribution. This effect should not be ignored when attempting to calculate the light fluence in objects (e.g. the head) in which there is a clear layer. Accurate modelling of these regions therefore needs to be carried out.

Our results show that, as might be expected, the diffusion theory alone is not very good at modelling clear regions. It is instructive to note its degree of inaccuracy. The hybrid model provides a good approximation to the experimental data and to the Monte Carlo results, especially when the same boundary conditions are used. The small amount of disagreement between the models is probably due to the approximation for the angular variation of emergent light not being exact. The exact angular dependence will depend on the position from the source; as can be seen in figure 6, equation (14) holds better at large

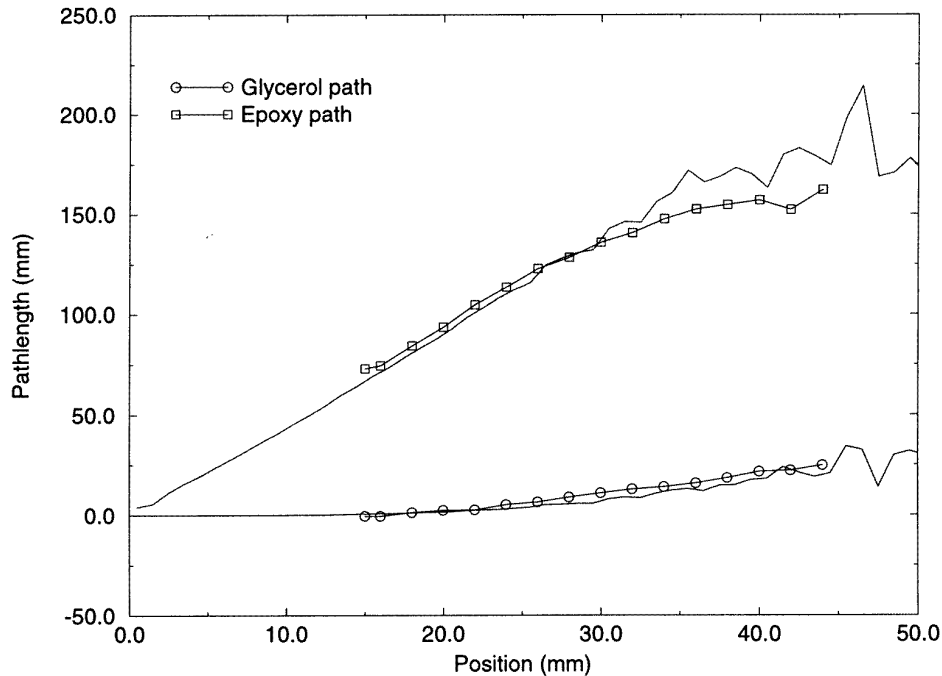


Figure 10. The pathlengths in the scattering and clear media as a function of fibre spacing measured from attenuation spectra compared to calculations from the Monte Carlo model for the case of a 1 mm clear layer.

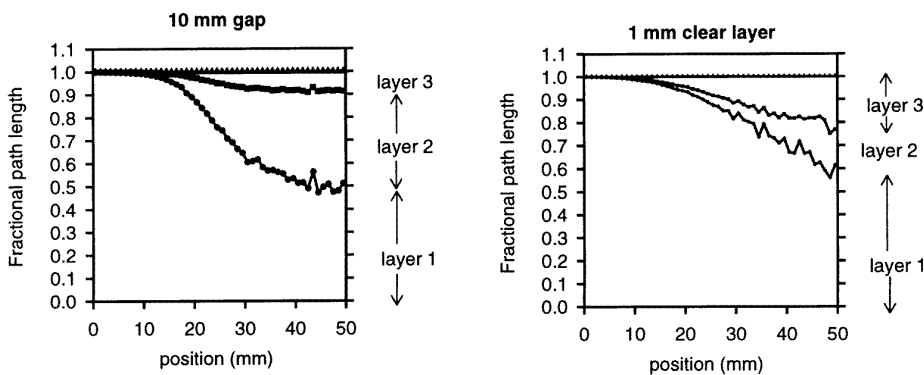


Figure 11. The fractional pathlength through the different layers of the phantom as a function of fibre spacing as calculated by the Monte Carlo model.

distances away from the source.

In all of the models, the refractive index difference between the scattering regions and the clear regions is ignored. This could be addressed in future, although it is unlikely to have a large effect on the light distribution, unless the refractive index difference between the two regions is large. This is not the case for CSF/brain tissue.

The hybrid model could be extended for use in combination with a finite-element

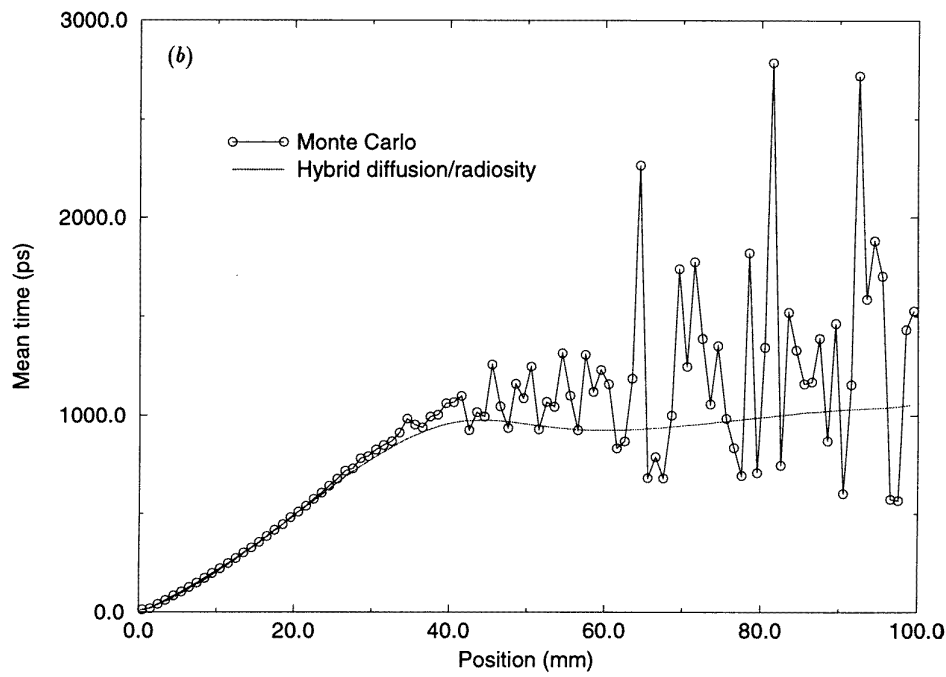
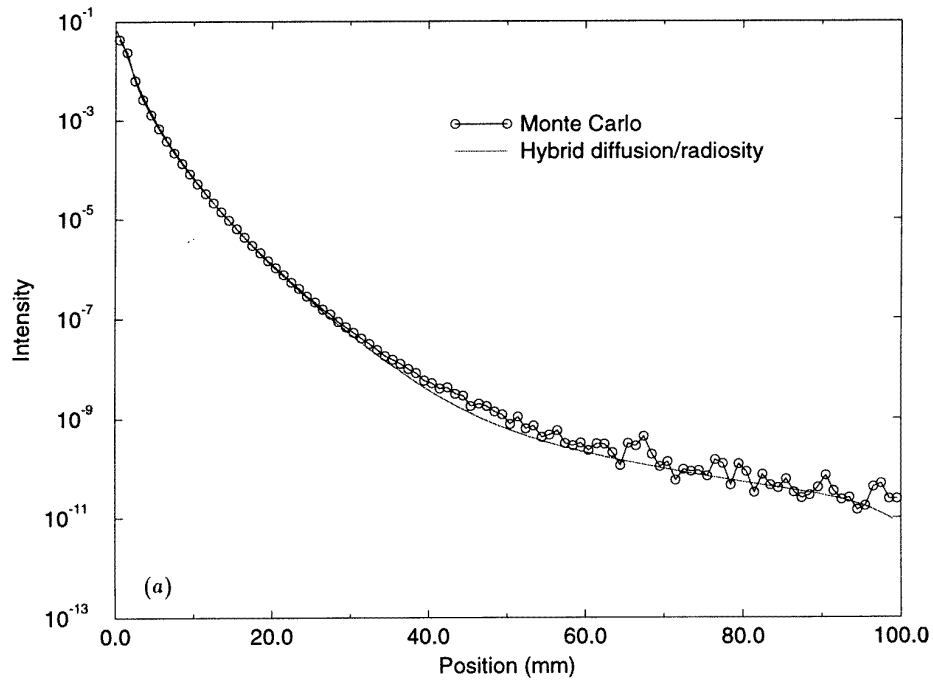


Figure 12. A comparison between (a) the reflected intensity and (b) the mean time of flight as a function of fibre spacing predicted by the Monte Carlo and hybrid diffusion–radiosity models for a 1 mm clear layer.

solution of the diffusion equation. This would have the advantage that more complex geometries could be investigated. At the moment, we have only a two-dimensional finite-element model, but it is hoped that in the near future the finite-element model will be extended to a three-dimensional geometry which should allow modelling of light transport in a model of the head. The finite-element model would also allow the use of different boundary conditions for different faces, e.g. a partially reflecting boundary condition for the edge facing the air and an extrapolated condition for the edge facing the clear layer.

Finally, the measurements made on a simple slab phantom indicate that in NIR spectroscopy of the adult head the brain may only contribute 10–20% of the total pathlength. However, as stated earlier, NIR spectroscopy as practised in currently available clinical machines only measures variations in signal, and, since the CSF and skull have only small variations in their chromophores, the contribution of the brain to the measured signal is likely to be larger. It should also be noted that the head is not slablike, and anatomically correct modelling of the head should be carried out to determine the actual light penetration into the brain.

Acknowledgments

The authors gratefully acknowledge the support of the EPSRC (grant GR/K07386), Action Research and Hamamatsu Photonics KK. Some of these data were presented earlier this year at an SPIE conference entitled *Optical Tomography, Photon Migration and Spectroscopy of Tissue and Model Media: Theory, Human Studies and Instrumentation* in San Jose (Firbank et al 1995b).

References

- Arridge S R, Cope M and Delpy D T 1992 The theoretical basis for the determination of optical pathlengths in tissue: temporal and frequency analysis *Phys. Med. Biol.* **37** 1531–60
- Barbour R L, Graber H L, Aronson R and Lubowsky J 1991 Determination of macroscopic optical properties of multilayer random media by remote sensing *Proc. SPIE* **1431** 52–62
- Bruscaglioni P, Zaccanti G and Wei Q 1993 Transmission of a pulsed polarized light beam through thick turbid media: numerical results *Appl. Opt.* **32** 6142–50
- Cohen M F and Wallace J R 1993 *Radiosity and Realistic Image Synthesis* (London: Academic)
- Cope M, Delpy D T, Reynolds E O R, Wray S, Wyatt J S and van der Zee P 1988 Methods of quantitating cerebral near infrared spectroscopy data *Adv. Exp. Med. Biol.* **222** 183–9
- Cope M, Delpy D T, Wray S, Wyatt J S and Reynolds E O R 1989 A CCD spectrometer to quantitate the concentration of chromophores in living tissue utilising the absorption peak of water at 975 nm *Adv. Exp. Med. Biol.* **247** 33–40
- De Blasi R A, Cope M, Elwell C E, Safoue F and Ferrari M 1993 Noninvasive measurement of human forearm oxygen consumption by near infrared spectroscopy *Eur. J. Appl. Physiol.* **67** 20–5
- Edwards A D, Wyatt J S, Richardson C E, Delpy D T, Cope M and Reynolds E O R 1988 Cotside measurement of cerebral blood flow in ill newborn infants by near infrared spectroscopy *Lancet* **2** 770–1
- Elwell C E, Owen-Reece H, Cope M, Wyatt J S, Edwards A D, Delpy D T and Reynolds E O R 1993 Measurement of adult haemodynamics using near infrared spectroscopy *Acta Neurochir. Suppl.* **59** 74–80
- Farrell T J and Patterson M S 1992 A diffusion theory model of spatially resolved, steady state diffuse reflectance for the noninvasive determination of tissue optical properties *in vivo Med. Phys.* **19** 879–88
- Firbank M 1994 The design, calibration and usage of a solid scattering and absorbing phantom for near infra red spectroscopy *PhD Thesis* University of London
- Firbank M, Oda M and Delpy D T 1995a An improved design for a stable and reproducible phantom material for use in near infra red spectroscopy and imaging *Phys. Med. Biol.* **40** 955–61
- Firbank M, Schweiger M and Delpy D T 1995b Investigation of ‘light piping’ through clear regions of scattering objects *Proc. SPIE* **2389** 167–3

- Flock S T, Patterson M S, Wilson B C and Wyman D R 1989 Monte Carlo modelling of light propagation in highly scattering tissues *IEEE Trans. Biomed. Eng.* **BME-36** 1162–73
- Hale G M and Query M R 1973 Optical constants of water in the 200 nm to 200 μ m wavelength region *Appl. Opt.* **12** 555–63
- Hampson N B and Piantadosi C A 1988 Near infra red monitoring of human skeletal muscle oxygenation during forearm ischaemia *J. Appl. Physiol.* **64** 2449–57
- Haselgrove J C, Schotland J C and Leigh J S 1992 Long term behavior of photon diffusion in an absorbing medium: application to time resolved spectroscopy *Appl. Opt.* **31** 2678–83
- Haskell R C, Svaasand L O, Tsay T-T, Feng T-C, McAdams M S and Tromberg B J 1994 Boundary conditions for the diffusion equation in radiative transfer *J. Opt. Soc. Am. A* **11** 2727–41
- Hiraoka M, Firbank M, Essenpreis M, Cope M, Arridge SR, van der Zee P and Delpy D T 1993 A Monte Carlo investigation of optical pathlength in inhomogeneous tissue and its application to near infrared spectroscopy *Phys. Med. Biol.* **38** 1859–76
- Key H, Davies E R, Jackson P C and Wells P N T 1991 Monte Carlo modelling of light propagation in breast tissue *Phys. Med. Biol.* **36** 591–602
- Matcher S J, Kirkpatrick P, Nahid K, Cope M and Delpy D T 1995 Absolute quantification methods in tissue near infrared spectroscopy *SPIE* **2389** 486–95
- Mihales D 1978 *Stellar Atmospheres* (New York: Freeman) ch 2
- Moulton J D 1990 Diffusion modelling of picosecond laser pulse propagation in turbid media *ME Thesis* McMaster University, Ontario
- Patterson M S, Chance B and Wilson B C 1989 Time resolved reflectance and transmittance for the non invasive measurements of tissue optical properties *Appl. Opt.* **28** 2331–6
- Peebles D M, Edwards A D, Wyatt J S, Bishop A P, Cope M, Delpy D T and Reynolds E O R 1992 Changes in human fetal cerebral haemoglobin concentration and oxygenation during labour measured by near infrared spectroscopy *Am. J. Obstet. Gynecol.* **166** 1369–73
- Schweiger M, Arridge S R and Delpy D T 1993 Application of the finite element method for the forward and inverse models in optical tomography *J. Math. Imaging Vision* **3** 263–83
- van Gemert M J C, Jacques S L, Sterenborg H J C M and Star W M 1989 Skin optics *IEEE Trans. Biomed. Eng.* **36** 1146–54
- Wyatt J S, Cope M, Delpy D T, Wray S and Reynolds E O R 1986 Quantitation of cerebral oxygenation and haemodynamics in sick newborn infants by near infrared spectroscopy *Lancet* **8515** 1063–6